



# Multipoint Observations and Modeling of the 2021 November 4 Forbush Decrease Using Solar Orbiter, CSES-01, and Ground-based Neutron Monitor Data

Simone Benella<sup>1</sup> , Monica Laurenza<sup>1</sup> , Matteo Martucci<sup>2</sup> , David Ruffolo<sup>3</sup> , Qiang Hu<sup>4</sup> , Georgios Nicolaou<sup>5</sup> , Christopher J. Owen<sup>5</sup> , Mirko Stumpo<sup>1</sup> , Christina Plainaki<sup>6,7</sup> , Francesco Palma<sup>2</sup> , Mirko Piersanti<sup>8</sup> , Matteo Sorbara<sup>2,9</sup> , Alessandro Sotgiu<sup>2</sup> , and Roberta Sparvoli<sup>2,9</sup>

<sup>1</sup> INAF—Institute for Space Astrophysics and Planetology, Via del Fosso del Cavaliere 100, 00133, Rome, Italy; [simone.benella@inaf.it](mailto:simone.benella@inaf.it)

<sup>2</sup> INFN—Sezione di Roma Tor Vergata, Via della Ricerca Scientifica 1, 00133, Rome, Italy

<sup>3</sup> Department of Physics, Faculty of Science, Mahidol University, Bangkok 10400, Thailand

<sup>4</sup> Department of Space Science, and Center for Space Plasma and Aeronomic Research, The University of Alabama in Huntsville, 35899, Huntsville, AL, USA

<sup>5</sup> Mullard Space Science Laboratory, University College London, Holmbury Saint Mary, Dorking, Surrey, RH5 6NT, UK

<sup>6</sup> Max Planck Institute for Solar System Research, Justus-von-Liebig-Weg 3, 37077 Göttingen, Germany

<sup>7</sup> Italian Space Agency, Via del Politecnico 1, 00133, Rome, Italy

<sup>8</sup> Department of Physical and Chemical Sciences, University of L'Aquila, 67100, L'Aquila, Italy

<sup>9</sup> Department of Physics, University of Rome Tor Vergata, Via della Ricerca Scientifica 1, 00133, Rome, Italy

Received 2025 March 21; revised 2025 April 24; accepted 2025 April 30; published 2025 June 12

## Abstract

During their propagation in the heliosphere, interplanetary coronal mass ejections (ICMEs) interact with galactic cosmic ray (GCR) particles, modifying their spectrum and driving anisotropies. We analyze the first large Forbush decrease (FD) of Solar Cycle 25 on 2021 November 3–5 by using multipoint in situ observations and neutron monitors to study the association between FD characteristics and ICME. We use the Grad–Shafranov reconstruction to infer the magnetic field configuration of the ICME. We model the neutron monitor response through primary spectrum and anisotropy. The primary spectrum is parameterized with the force-field approximation and the anisotropy is modeled through a spherical harmonic expansion. We optimize the model parameters during the FD by using ground-based observations provided by the worldwide neutron-monitor network. The model's results are compared with space-based measurements of the differential proton flux measured by the HEPD-01 detector on board the CSES-01 satellite and of the integral counts of both the High-Energy Particle Detector (HEPD-01) and the High Energy Telescope on board the Solar Orbiter. Anisotropy develops during the ICME passage, within the magnetic flux rope (MFR) and is found to be bidirectional. The force-field parameterization of the primary GCR fluxes based on ground-based measurements is found to be in very good agreement with spacecraft observations in the sub-GeV range. The GCR anisotropy obtained by fitting the model to ground-based observations is consistent with interplanetary magnetic field observations. The results suggest that the local magnetic field has a substantial axial component that is aligned to the MFR axis, and determines the GCR anisotropy at the typical neutron monitor energies.

*Unified Astronomy Thesaurus concepts:* Galactic cosmic rays (567); Solar coronal mass ejections (310); Forbush effect (546)

## 1. Introduction

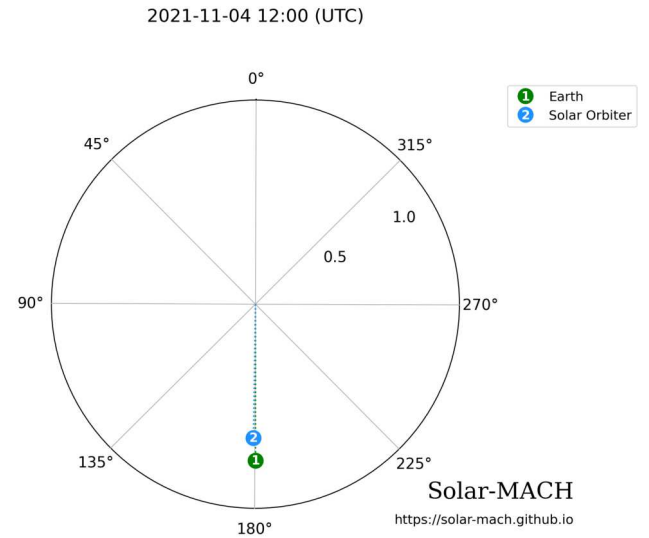
When cosmic-ray particles accelerated in the Galaxy reach the heliosphere, they interact with the solar wind carrying the interplanetary magnetic field, turbulence, and several types of transient magnetic structures of solar or interplanetary origin. The result is the well-known modulation effect of galactic cosmic rays (GCRs), producing particle density variations from very large timescales (say decades) to very small ones (e.g., hours) (L. J. Gleeson & W. I. Axford 1968; M. S. Potgieter 2013). On the short timescales, modulation of the background GCR intensity is produced by quasi-periodic or sporadic events, such as corotating stream interaction regions (CIR) and interplanetary coronal mass ejections (ICMEs). The latter, in particular, have been demonstrated by a substantial body of long-term research to be highly effective in producing pronounced GCR intensity reductions, known as Forbush

decreases (FD; S. E. Forbush 1937). ICMEs often propagate at a considerably high speed with respect to the background solar wind, thus being preceded by intense shock waves associated with their emission and propagation. Moreover, they develop a thick layer of shocked and compressed plasma during the propagation: the sheath region. These ingredients constitute the underlying basis for the typical two-step time profile of FDs (H. V. Cane 2000). The first step is produced by shock, acting as a propagating barrier (G. Wibberenz et al. 1998; G. Wibberenz & H. V. Cane 2000), strengthened by the enhanced plasma density and turbulence of the sheath; whereas the second step is associated with the magnetic flux rope (MFR), a structure characterized by a colder and more rarefied plasma and a pronounced helical magnetic configuration, representing the core of the ICME (L. F. Burlaga et al. 1982). Although this description represents an idealized simplification and the nature of FDs may be significantly more complex (A. P. Jordan et al. 2011), such signatures in the GCR intensity are routinely observed at the Earth during the passage of ICMEs and have also been documented beyond in the solar system (K. I. Paularena et al. 2001; O. Witasse et al. 2017; R. M. Winslow et al. 2018).



Original content from this work may be used under the terms of the [Creative Commons Attribution 4.0 licence](https://creativecommons.org/licenses/by/4.0/). Any further distribution of this work must maintain attribution to the author(s) and the title of the work, journal citation and DOI.

Space-based observations of FDs are of great importance in order to assess the effect of ICMEs in modulating primary GCR particles. These measurements allow us to study the relation between different phases of the disturbance and the resultant fine structure in cosmic-ray variations as a function of time and energy, the dependence on the position in multi-spacecraft studies, and finally the effect of the radial expansion of the ICME (J. A. Lockwood et al. 1991; H. V. Cane et al. 1994; J. L. Freiherr von Forstner et al. 2018, 2021). Ground-based observations of GCR intensity variations also provide fundamental elements in the study of the formation and anisotropy of FDs during ICMEs (N. Iucci et al. 1989; H. V. Cane 2000; M. Dumbović et al. 2018; A. S. Petukhova et al. 2019; M. Papailiou et al. 2020). Ground-based observations are traditionally carried out by neutron monitors (NMs), which are designed to detect the nucleonic component of secondary particles produced by the interaction between primary GCRs and atmospheric nuclei (J. A. Simpson 2000), and by muon detectors (K. Munakata et al. 2000). Multi-directional observations supplied by the worldwide NM network have long been used thanks to their ability to provide fundamental information about the energy dependence and anisotropy of cosmic-ray transient variations. The fundamental principle underlying their combined use is that cosmic-ray variations at a given location arise from two main contributions: an overall change in the omnidirectional intensity and a more local variation induced by the GCR anisotropy. Taking advantage of the different geographic positions, and thus different particle energy sensitivity due to geomagnetic cutoff, and the different directions of viewing of the detectors around the globe, these aspects can be precisely addressed during periods of enhanced GCR intensity variations, such as ground-level enhancements (GLEs) or FDs. Examples of the application of these principles include ground-based GLE modeling (M. A. Shea & D. F. Smart 1982; J. L. Cramp et al. 1997; J. W. Bieber et al. 2002; D. J. Bombardieri et al. 2006; C. Plainaki et al. 2009, 2014; A. L. Mishev et al. 2014; A. Mishev et al. 2018) and FD (e.g., see J. W. Bieber & P. Evenson 1998; A. V. Belov et al. 2018; U. Torkermpun et al. 2018; K. Munakata et al. 2022, and references therein). The retrieval of the primary spectrum and anisotropy of a FD event from ground-based observations constitutes a key aspect that has been addressed for a long time through different models (J. W. Bieber & P. Evenson 1998; K. Munakata et al. 2006; T. Kuwabara et al. 2009; I. G. Usoskin et al. 2015; A. V. Belov et al. 2018; U. Torkermpun et al. 2018; A. Mishev et al. 2024). All of these studies are important for understanding the response of ground-based detectors to primary GCR variations and for providing insights on the physics of FD formation in association with the passage of ICMEs. From an observational point of view, many of these investigations are carried out based on case studies of interest that have peculiar features, since their actual time evolution can vary significantly from the canonical two-step decrease model (A. P. Jordan et al. 2011). In this context, we perform an in-depth analysis of multipoint observations of the first large FD in Solar Cycle 25, as well as modeling of the primary GCR flux modulation in the sub-GeV energy range by using ground-based observations gathered by the NM network, extending previous studies more oriented toward higher energies. Moreover, we investigate the connection between the obtained FD anisotropy and the main characteristics of the MFR of the



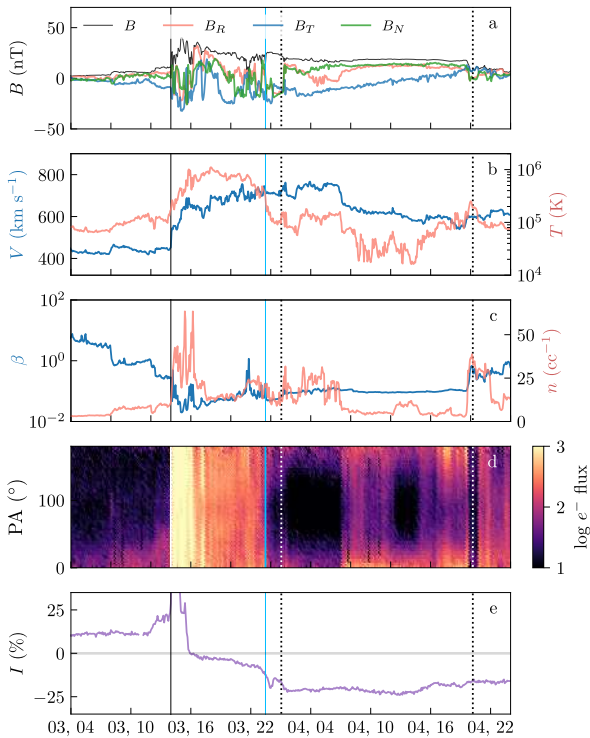
**Figure 1.** Position of SO and Earth during the ICME passage on 2021 November 4 obtained from the Solar-MACH tool (J. Gieseler et al. 2023).

ICME. A realistic configuration of the MFR based on in situ observations of plasma and magnetic field can be obtained by applying the Grad-Shafranov (GS) reconstruction method (see S. Q. Hu 2017, for a review). In previous works, the relevance of precise knowledge of the MFR configuration in association with fine-structure temporal profiles of FDs has been emphasized with the joined use of GS reconstruction and cosmic-ray test-particle simulations (S. Benella et al. 2020, 2021). However, the relevance of these studies is confined to cases of FD events observed in space in association with stealth ICMEs, i.e., when the global particle decrease is induced by the MFR. In this work, we use the GS reconstruction to explore the connection between the GCR anisotropy and the global MFR geometry.

## 2. Data Description

### 2.1. Solar Orbiter Observations

During the period 2021 November 3–5 an ICME passed through the Solar Orbiter (SO) spacecraft, which was located at a radial distance of 0.85 au, in radial alignment with the Earth, as shown in Figure 1. This configuration is favorable for studying from multiple locations the main characteristics of the event, such as the presence of energetic storm particles associated with the shock wave (F. Chiappetta et al. 2023). The shock of the ICME reached SO on 2021 November 3 at 14:00 UTC, followed by a large-scale MFR in the time interval 2021 November 4 at 01:03 UTC to 20:13 UTC. During this period, the MAG instrument (T. S. Horbury et al. 2020) on board SO gathered magnetic field data with 0.125 s time resolution (Figure 2(a)) and the Proton Alpha Sensor (PAS) integrated in the Solar Wind Analyzer plasma suite (C. J. Owen et al. 2020) provided plasma data at 4 s resolution (Figures 2(b) and (c)). Figure 2(d) shows the pitch-angle distribution obtained by the Electron Analyser System (EAS) for electrons with energies  $>69$  eV. The vertical lines indicate the interplanetary shock passage, detectable by the discontinuities observed in magnetic field and plasma parameters, and the MFR time interval. The time interval between the shock and the MFR constitutes a complex region with enhanced fluctuations of the magnetic



**Figure 2.** From top to bottom: (a) SO/MAG magnetic field measurements in RTN reference frame along with magnetic field magnitude; (b) SO/PAS data of solar wind speed and temperature; (c) SO/PAS data of plasma density and plasma beta; (d) SO/EAS  $>69$  eV electron pitch-angle distribution; and (e) SO/HET particle intensity variation  $>12$  MeV. Vertical lines marks shock arrival time (solid black) small scale MFR onset (solid blue), and the large-scale MFR transit time (dotted black). Time labels indicate day and hour (dd, HH) of 2021 November.

field components, increased proton bulk density, velocity, and temperature, and a sudden increase of electron flux in all directions behind the shock. The MFR time interval reported in the figure has been obtained from L1 data as discussed in Section 2.2. The two High Energy Telescopes (HETs) of the Energetic Particle Detector suite (J. Rodríguez-Pacheco et al. 2020) can provide measurements of high-energy particle count rates in single count mode at energies greater than  $\sim 12$  MeV, as comprehensively discussed in J. L. Freiherr von Forstner et al. (2021). Each HET unit consists of four counters: two with high-gain and two with low-gain channels. In order to obtain the integrated omnidirectional GCR intensity with good statistics of particle counts per second, we summed the count rates of high-gain channels following the method illustrated by J. L. Freiherr von Forstner et al. (2021) (see also A. Aran et al. 2021). High-energy particle intensity variations observed by SO are reported in Figure 2(e). The HET count rate exhibits a sharp increase at the shock arrival followed by an intense two-step decrease, the first in correspondence of the sheath region and the second due to the MFR. This particle increase can be associated with energetic particles locally accelerated and/or trapped by the shock, i.e., the so-called energetic storm particle phase of a solar energetic particle (SEP) event. In fact, the November FD event was preceded by a GLE observed at Earth on 2021 October 28, with SEP flux increases that last several days (e.g., see A. L. Mishev et al. 2022; A. Papaioannou et al. 2022; M. Martucci et al. 2023a). In order to exclude possible SEP contamination in estimating the background cosmic-ray intensity, we select a reference period well before the GLE,

between 00:00 UTC and 12:00 UTC on 2021 October 23. The resulting FD amplitude measured by HET at energies  $>12$  MeV is 23.3% with respect to the average value during this period.

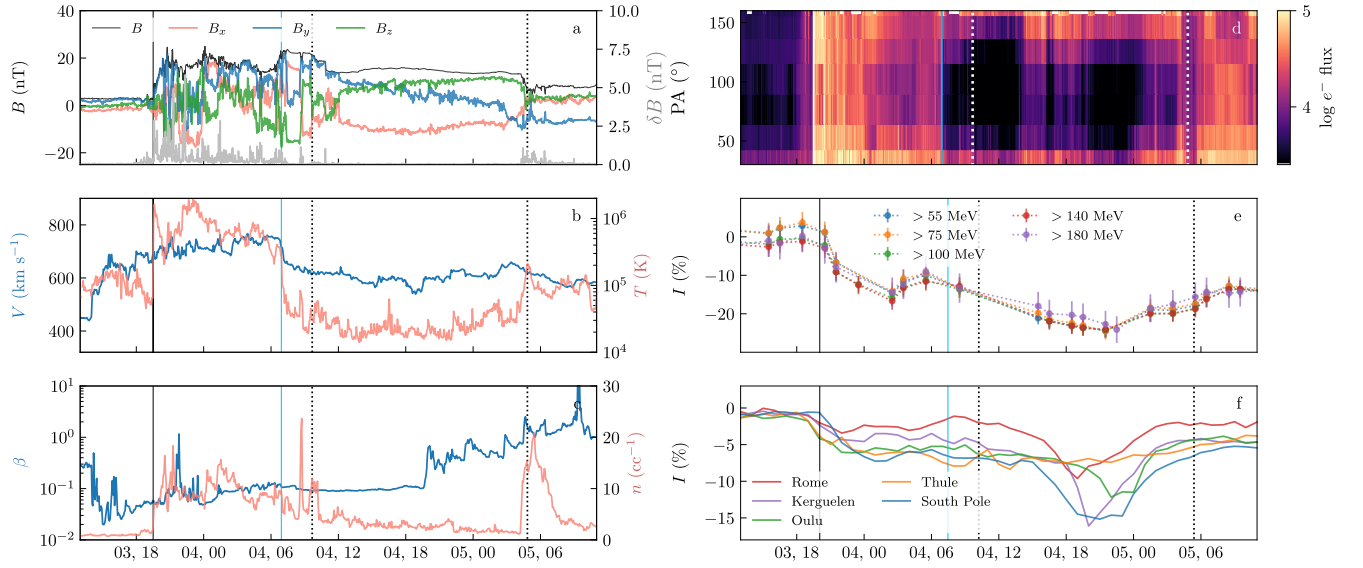
## 2.2. L1 and Earth Observations

After approximately 5.3 hr of observation at SO, the shock reached the Earth followed by the ICME, and it was detected by the Wind spacecraft orbiting around the L1 Lagrangian libration point (Figure 3). The shock arrival time at L1 is at 19:30 UTC on November 3 and the MFR passage starts at 09:40 UTC on November 4 and ends at 04:50 UTC on November 5. This structure is representative of the large-scale MFR within the ICME. On the other hand, by carefully inspecting Figure 3, we note the presence of smaller MFRs after 07:00 UTC on November 4 preceding the large-scale structure, characterized by a lowering in temperature and plasma beta, and by smooth magnetic field during which field fluctuations are inhibited. The large-scale MFR crossed the Earth with a stable speed of approximately  $673 \text{ km s}^{-1}$ . The pitch-angle distribution of the electron strahl within, e.g., at the energy of 200 eV, shows typical signatures of bidirectional flux (L. F. E. Burlaga 1991) observed in closed-loop structures such as MFRs (Figure 3(d)), with a pattern very similar to the one previously observed by SO/EAS, Figure 2(d).

Concerning space-based observation of the FD in the near-Earth environment, we use data collected by the High-Energy Particle Detector (HEPD-01) on board the China Seismo-Electromagnetic Satellite (CSES-01; X. Shen et al. 2018). Launched in 2018, CSES-01 is orbiting at an altitude of approximately 500 km in a quasi-polar, Sun-synchronous orbit. Thanks to HEPD-01, it provides accurate measurements of galactic, trapped, and solar particles (P. Picozza et al. 2019; S. Bartocci et al. 2020; M. Martucci et al. 2022, 2023b). The instrument has been completely developed and assembled in Italy and it has been optimized for measuring electrons in the 3–100 MeV energy range, and protons and light nuclei in the 30–300 MeV energy range. In Figure 3(e), we show the particle intensity variations observed by HEPD-01 with different low energy thresholds. These intensities are calculated from the rate extracted from instrument counters—or ratemeters—which provide information on the particle energy above a certain threshold but which do not separate different species or arrival angle. The advantage is to obtain high-cadence count rates with a high efficiency. As reported in Figure 3(e), HEPD-01 measured a pronounced FD reaching amplitudes of about 22%–24% for all the measured energies up to  $>180$  MeV.

Finally, Figure 3(f) displays ground-based NM observations from five selected detectors. These NMs are located in different geographic positions and at different altitudes. Although the FD is easily identified, it appears quite different depending on the observing point. For instance, a small though very clear decrease is detected at the Study of Variations of Cosmic-Ray Intensity Observatory (SVIRCO) in Rome, because of the higher geomagnetic cutoff with respect to the other reported stations. At high-latitude stations, both in the northern (Oulu) and southern (Kerguelen, South Pole) hemisphere, the FD appears to be significantly more intense. However, the nearly polar station Thule, located in the geomagnetic north, provides data with a contrasting trend, where the only visible the first step of the FD. This brief





**Figure 3.** Magnetic field and plasma parameters observed by Wind: (a) magnetic field geocentric solar ecliptic components along with IMF magnitude and rms  $\delta B$ , (b) flow speed, plasma temperature, (c) plasma beta, density, and (d) 200 eV electron pitch-angle distribution. CSES/HEPD-01 intensity variations of the integrated counts with cutoff at different energies are reported in the panel (e), and ground-based intensity variations from NMs in (f). Vertical lines indicate the shock arrival time (solid black), the small MFR time (solid blue), and the large-scale MFR transit time (dotted black). Reference times in panels (e) and (f) are shifted of the average time of propagation to the Earth bow shock of approximately 33 minutes.

qualitative description of NM observations, complemented by a substantial analysis in the following section, provides insight into the actual complexity of the event and highlights how the anisotropy caused by the passage of the MFR is immediately apparent. When an MFR propagates in the interplanetary space, it induces an anisotropic distribution of GCR particles that can be detected at Earth through the global network of NMs (e.g., see A. V. Belov et al. 2018, and references therein). This anisotropy typically manifests as a directional excess or deficit of GCR counts, resulting in notably distinct profiles of the particle intensities measured at the different geographic positions of the worldwide NM network.

### 3. Grad-Shafranov Reconstruction

The nearly 3D configuration of the MFR is obtained by performing the GS reconstruction (L. N. Hau & B. U. Ö. Sonnerup 1999; S. Q. Hu 2017). The GS reconstruction method is based on the assumption of axisymmetric plasma equilibrium and provides the MFR configuration by using data from a single spacecraft (Q. Hu & B. U. Ö. Sonnerup 2002). The GS equation of a 2D steady plasma structure can be written in Cartesian coordinates as

$$\frac{\partial^2 A}{\partial x^2} + \frac{\partial^2 A}{\partial y^2} = -\mu_0 \frac{d}{dA} \left( p + \frac{B_z^2}{2\mu_0} \right), \quad (1)$$

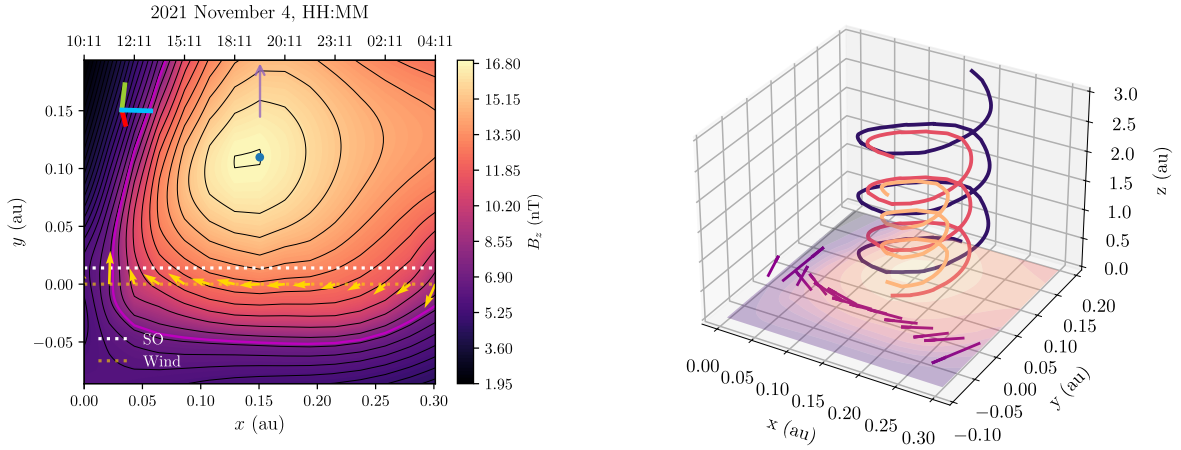
where  $A$  is the potential vector of the magnetic field  $B$ ,  $p$  is the plasma pressure, and  $\mu_0$  is the vacuum magnetic permeability. The two Cartesian coordinates  $x$ - $y$  describe the plane where the magnetic structure lies. The direction  $z$ , normal to the plane, identifies the symmetry axis along which the structure is translation invariant, i.e.,  $\partial/\partial z = 0$ . The GS reconstruction method can be summarized in three main steps:

1. Searching for the velocity vector describing the constant propagation of the plasma structure: de Hoffmann-Teller (HT) analysis (F. de Hoffmann & E. Teller 1950);

2. Identifying the best invariant axis  $z$  through an optimization procedure based on single spacecraft data sample (Q. Hu & B. U. Ö. Sonnerup 2002);
3. Inferring the potential vector on the  $x$ - $y$  plane through a second-order Taylor expansion in which Equation (1) is assumed to be valid (L. N. Hau & B. U. Ö. Sonnerup 1999).

In this work, we start from data gathered by Wind at L1, by using 1 s resolution magnetic field data from the Magnetic Field Investigation (R. P. Lepping et al. 1995) instrument and 4 s resolution plasma observations provided by the Solar Wind Experiment (K. W. Ogilvie et al. 1995). The data interval selected for the reconstruction is indicated by vertical dashed lines in Figure 3. The HT velocity obtained from the Wind data is  $V_{HT} = (-669, 15, 68) \text{ km s}^{-1}$  in the geocentric solar ecliptic (GSE) frame, and the orientation of the MFR  $z$ -axis is  $\lambda_{MFR} = [59 \pm 8]^\circ$  and  $\theta_{MFR} = [108 \pm 3]^\circ$ , where  $\lambda$  and  $\phi$  indicate the GSE latitude and longitude, respectively. Figure 4 (left panel) shows the reconstruction obtained for the MFR of 2021 November 4–5. The color map shows the intensity of the axial magnetic field, whereas the black lines indicate isopotential curves. The trajectories of SO and Wind are reported in the reference frame of the reconstruction and the Wind magnetic field measurements of the transverse magnetic field are indicated by yellow arrows, showing the smooth rotation of the magnetic field when the spacecraft traverses the flux rope. The blue dot located at (0.15, 0.11) au indicates the center of the MFR, thus having an “impact factor”—viz., the distance between MFR center and the observer—of approximately 0.11 au. A three-dimensional visualization of the obtained MFR along with the transverse magnetic field rotation measured by Wind is reported in the right panel of Figure 4.

The availability of MAG measurements from SO allows us to validate the reconstruction obtained from Wind (C. Möstl et al. 2009). By shifting the MFR obtained through the GS reconstruction of a time interval  $\Delta\tau = \Delta r/V_{HT} = 8.6 \text{ hr}$ , where  $\Delta r = 0.14 \text{ au}$  is the spacecraft distance and

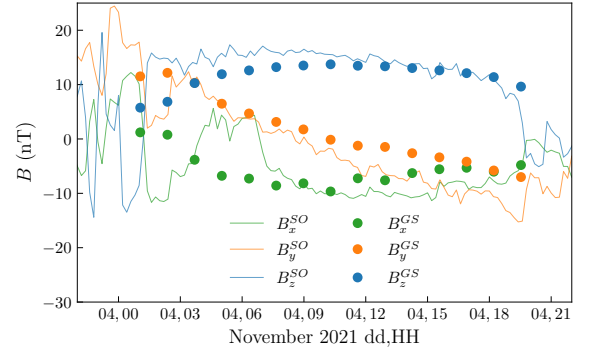


**Figure 4.** Left: GS reconstruction of the 2021 November event with Wind (yellow dots) and SO (white dots) spacecraft paths across the MFR. The color map indicates the intensity of the axial component of the magnetic field along with isopotential curves (black lines). The contour highlighted in magenta indicates the boundaries of the MFR and the yellow arrows are Wind observations of the transverse magnetic field. A projection of the GSE reference frame is reported in the corner ( $X_{GSE}$  in light blue,  $Y_{GSE}$  in green, and  $Z_{GSE}$  in red). Right: A 3D representation of the reconstructed MFR. Helical lines emphasize the three-dimensional structure of the flux rope whereas purple vectors are Wind magnetic field measurements highlighting the observed rotation of the transverse magnetic field.

$V_{HT} = 673 \text{ km s}^{-1}$  is indicative of the nearly constant propagation of the MFR, we can compare GS reconstruction outcomes with SO data. This comparison is reported in Figure 5, where GS reconstruction magnetic field values (circles) are interpolated along the SO trajectory within the MFR (Figure 4). SO data (solid lines) have been resampled at 15 minutes in order to highlight the smooth trend observed during the MFR. From this test we conclude that the structure obtained from the GS reconstruction is accurate in reproducing the large-scale trend of the MFR, also when back-propagated to the SO position, and that the expansion of the MFR, despite it is characterized by colder plasma at L1, is not distinctly observed, since the size of the structure at SO and at Wind is found to be similar.

#### 4. Forbush Decrease Model

In this section, we introduce a model which uses ground-based NM observations for retrieving the primary spectrum and the anisotropy of a FD. Given that FDs are a depletion of the background GCR intensity, the analytic form of the primary spectrum is chosen according to the Gleeson & Axford model (hereafter G&A; L. J. Gleeson & W. I. Axford 1968), so that the only parameter that appears in the primary spectrum is the modulation potential. The G&A model is based on the force-field approximation which, although grounded in physical principles, sometimes lacks a definitive physical interpretation of the modulation potential. As emphasized by I. G. Usoskin et al. (2015), the fundamental physical assumptions underpinning this approximation—e.g., quasi-steady solar wind expanding spherically—make it invalid over short timescales and/or under disturbed heliospheric conditions (R. A. Caballero-Lopez & H. Moraal 2004). Thus, it is generally accepted that the force-field model does not apply to transient events such as FDs. Nonetheless, the choice of using it as a simple mathematical tool to parameterize the GCR spectrum has been shown to be meaningful and to produce consistent results (e.g., see I. G. Usoskin et al. 2015). As in I. G. Usoskin et al. (2017),



**Figure 5.** Multispacecraft validation of the GS reconstruction. Circles represent the magnetic field components obtained from the GS reconstruction and solid lines are the SO magnetic field components resampled at 15 minutes and rotated in the reconstruction frame.

we assume the local interstellar particle spectrum to be

$$J_s^{\text{LIS}} = 2.7 \times 10^3 C_s \frac{E^{1.12}}{\beta} \left( \frac{E + 0.67}{1.67} \right)^{-3.93}, \quad (2)$$

where  $E$  is the particle relativistic kinetic energy,  $\beta = v/c$  is the ratio between the proton velocity and the speed of light, and  $C_s$  is a constant depending on the species  $s$  of primary particles (e.g.,  $C_p = 1$  and  $C_{\text{He}} = 0.3$  according to I. G. Usoskin et al. 2017). The modulation theory introduced by G&A allows to write the modulated primary proton spectrum at 1 au given the local interstellar spectrum through the following expression:

$$J_s(E, \phi) = J_s^{\text{LIS}}(E + \Phi) \frac{E_{\text{tot}}^2 - E_0^2}{(E_{\text{tot}} + \Phi)^2 - E_0^2}, \quad (3)$$

where  $E_{\text{tot}}$  is the total particle energy,  $E_0 = 0.938 \text{ GeV}$  is the proton rest mass and  $\Phi$  is the GCR mean energy loss defined as  $\Phi = \phi(eZ/A)$ , where  $\phi$  indicates the modulation potential,  $e$  the particle charge, and  $Z$  and  $A$  are the particle atomic and mass numbers, respectively. We define  $\Delta N(t) = N(t) - N_0$  as the difference between the count rate  $N(t)$  and a reference background  $N_0$ , and we indicate with  $\phi_0$  the modulation

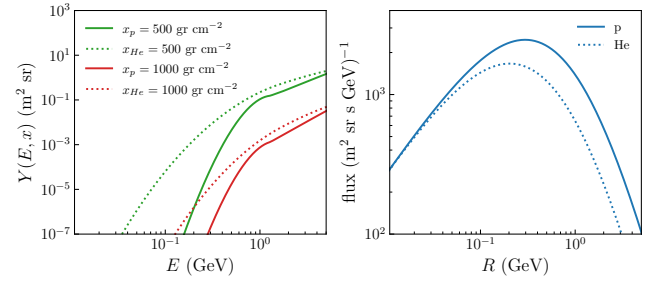
potential associated with the quiet GCR background preceding the event and with  $J_{0,s}$  the differential flux  $J_{0,s} = J_s(E, \phi_0)$ . The background GCR flux is assumed to be isotropic, whereas FD events are usually affected by the spatial configuration of the MFR producing the second-step decrease, which therefore is strongly anisotropic. For this reason, we introduce the time-dependent differential flux  $J_s[E, \phi(t)]$ , where the modulation potential  $\phi(t)$  is used to model the global omnidirectional flux attenuation due to the ICME's passage (I. G. Usoskin et al. 2015), which can be locally modulated by an anisotropy term  $\mathcal{A}$ . The anisotropy term is modeled through a spherical harmonics expansion as follows

$$\mathcal{A}(\lambda, \theta, t) = \sum_{l=0}^2 \sum_{m=-l}^l a_{lm}(t) Y_{lm}^R(\lambda', \theta), \quad (4)$$

where  $Y_{lm}^R$  indicates the real spherical harmonics of order  $l$  depending on the asymptotic colatitude  $\lambda' = \pi/2 - \lambda$  and longitude  $\theta$  at a given particle energy, and the expansion coefficients  $a_{lm}$  are parameters of the model to be fitted to the NM data. The spherical harmonic expansion includes dipolar and quadrupolar terms, since the event examined in this work is characterized by a large amplitude bidirectional anisotropy, as extensively shown by K. Munakata et al. (2022). Since the background is assumed to be isotropic, the factor  $\mathcal{A}(\lambda, \theta, t)$  acts on the modulation of the primary flux during the MFR passage, thus inferring important information about its geometry by using the NM viewing directions. Then, we can write the intensity variation measured by a NM with energy cutoff  $E_c$  at altitude  $h$  at the time  $t$  as

$$\begin{aligned} & \frac{\Delta N(E_c, h, t)}{N_0} \\ &= 1 - \frac{\sum_s \int_{E_c} J_s[E, \phi(t)] \mathcal{A}(\lambda, \theta, t) W_s(E, x) dE}{\sum_s \int_{E_c} J_{0,s}(E, \phi_0) W_s(E, x) dE}, \end{aligned} \quad (5)$$

where  $W_s(E, h)$  is the response function of the particle  $s = p, \text{He}$ , representative of the coupling of secondary nucleons detected at ground with primary incident GCR particles, as well as the efficiency of the detector in revealing secondaries. The NM response function indicates the efficiency of primary particles of a given energy in generating secondary nucleons at a given atmospheric depth (altitude) and at a fixed level of long-term modulation of the GCR background. Since NMs can be considered as omnidirectional detectors monitoring the nearly vertical incident primaries on average, the production of secondaries is modeled by using the updated NM yield function parameterized by A. L. Mishev et al. (2020) for protons and Helium nuclei. Examples of yield functions for different atmospheric depths  $x$  are illustrated in the left panel of Figure 6. The long-term attenuation effect is included by convolving the yield function with the long-term modulated primary fluxes corresponding to the modulation potential  $\phi_0 = 360$  MV (Figure 6 right panel), obtained by fitting the HEPD-01 background energy spectrum (Section 5.1). All response functions are normalized by the total integral over  $E$  and given in  $\text{GeV}^{-1}$  units.



**Figure 6.** Left: Examples of yield function used in the model at two different atmospheric depths,  $x = 500 \text{ gr cm}^{-2}$  in green and  $x = 1000 \text{ gr cm}^{-2}$  (sea level) in red, for proton (solid lines) and Helium nuclei (dotted lines). Right: Background proton (solid) and Helium (dotted) spectra used in the MN response function obtained from the G&A model with  $\phi = 360$  MV.

**Table 1**  
Effective Vertical Cutoff Rigidity, Altitude, and Geographic Position of the NM Used in This Study

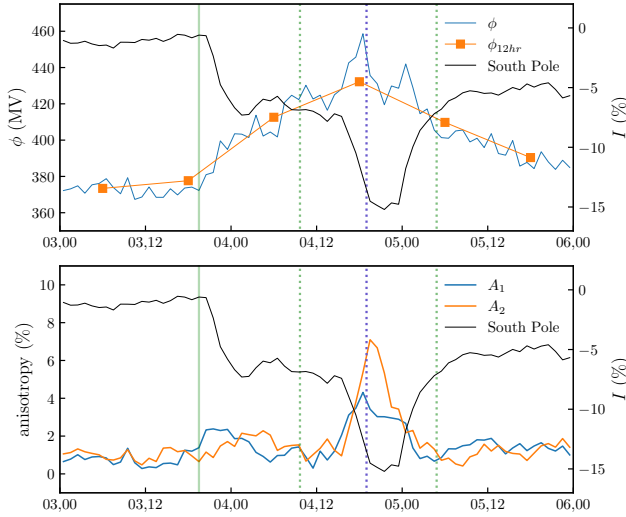
NM Station	$R_c$ (GV)	$h$ (m)	Lat (°)	Lon (°)
Terre Adelie	0.0	32	−66.65	240
Dome C	0.01	3233	−75.1	123.33
South Pole	0.1	2820	−90	N/A
Nain	0.3	46	56.55	−61.68
Jang Bogo	0.3	30	−74.6	164.2
Inuvik	0.3	21	68.36	−133.72
Thule	0.3	26	76.5	−68.7
Peawanuck	0.3	53	54.98	−85.44
Fort Smith	0.3	180	60.02	−111.93
Tixie Bay	0.48	0	71.36	128.54
Norilsk	0.63	0	69.26	88.05
Apatity	0.65	181	67.57	33.4
Oulu	0.8	15	65.05	25.47
Kerguelen	1.14	33	−49.35	70.25
Yakutsk	1.65	105	62.01	129.43
Newark	2.4	50	39.68	−75.75
Dourbes	3.18	225	50.1	4.60
Jungfrau-joch	4.5	3475	46.55	7.98
Baksan	5.6	1700	43.28	42.69
Almaty	5.9	897	43.13	76.55
Rome	6.27	0	41.86	12.47
Calma	6.95	708	40.56	−3.16
Mexico	8.2	2274	19.33	−99.18
Athens	8.53	260	37.97	23.78
Daejeon	11.22	200	36.24	127.22
Doi Inthanon	16.8	2560	18.59	98.49

## 5. Results

### 5.1. Primary Energy Spectrum

The initial differential energy spectrum  $J_{0,p}(E, \phi_0)$  has been obtained by fitting the G&A model over the differential proton spectrum obtained from HEPD-01 in a quiet period of 12 hr between 00:00 UTC and 12:00 UTC on 2021 October 23. As described above, the reference time interval is located several days before the FD in order to exclude the GLE that occurred on 2021 October 28 and was observed by the global NM network (A. L. Mishev et al. 2022) and by HEPD-01 (M. Martucci et al. 2023a). The modulation potential obtained for the background is  $\phi_0 = 360$  MV.

For the model best fit we used 26 NM stations, ensuring a comprehensive sky coverage of viewing directions. The detectors used are listed in Table 1, along with their cutoff

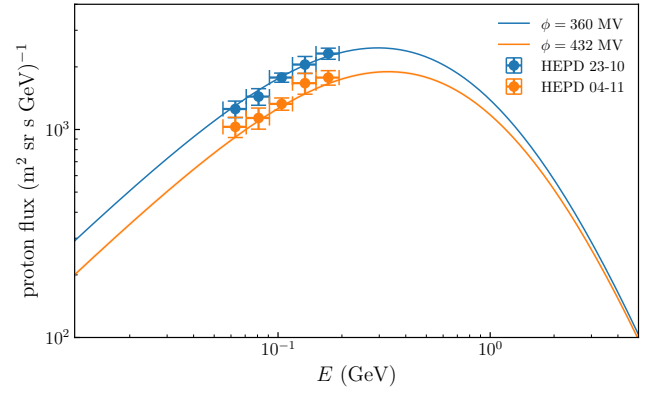


**Figure 7.** Top: Hourly (blue) and 12 hr averaged (orange) modulation potential. Bottom: Amplitudes of first-order (blue) and second-order (orange) anisotropy. Vertical green lines mark the shock arrival (solid) and the MFR interval (dotted). The purple dotted line indicates the time corresponding to the closest approach to the MFR core (see also Figure 4). The black line reported in both panels shows the GCR intensity variation measured by South Pole NM as reference.

rigidity  $R_c$ , altitude  $h$ , and geographic positions. According to Equations (3) and (4) the number of free parameters is 10: nine spherical harmonic coefficients  $a_{lm}$  and the modulation potential  $\phi$ . The asymptotic directions ( $\lambda$ ,  $\theta$ ) of each NM have been calculated in the  $[0, 100]$  GV rigidity range by using the international geomagnetic reference field (P. Alken et al. 2021) for the geomagnetic field and the external magnetospheric model TSY01 (N. A. Tsyganenko 2002a, 2022b; N. A. Tsyganenko et al. 2003). The particle trajectory computation has been performed by using the Open-Source Geomagnetosphere Propagation Tool (OTSO), recently introduced by N. Larsen et al. (2023). We initialized the TSY01 magnetospheric model by using hourly OMNIWeb<sup>10</sup> magnetic field and plasma data and we calculated the time-dependent asymptotic directions, on hourly basis, for the entire duration of the event. Finally, the optimization has been carried out through a nonlinear least-squares fit on hourly resolution NM data.

Figure 7 shows the results obtained from the optimization as a function of time between November 3 at 00:00 UTC and November 6 at 00:00 UTC. The top panel of Figure 7 shows the modulation potential  $\phi(t)$  in MV along with the GCR intensity variation observed by the South Pole NM. Starting from values close to  $\phi_0$ , the obtained  $\phi(t)$  shows an increase in correspondence with the first step of the FD associated with the shock transit time. Then, it increases toward the maximum reached during the MFR crossing time.

To test the proton primary spectrum predicted by the model during the main phase of the FD, we use differential proton spectra gathered by HEPD-01 in the energy range between 30 and 300 MeV. To have enough statistics for the differential spectrum, HEPD-01 proton fluxes are averaged over 12 hr time bins. As a consequence, the time series  $\phi(t)$  obtained from the optimization has been resampled accordingly, see Figure 7. In this fashion, we can compare the measured proton spectrum at



**Figure 8.** Comparison between the differential spectrum obtained from the model optimization (orange line) and the one measured by HEPD-01 during the main phase (orange circles) in the time interval ranging from November 4 at 12:00 to November 5 at 00:00. The blue solid line is the pre-event proton spectrum fitted on HEPD-01 observations (blue circles) in the interval 00:00-12:00 on October 23.

the dip of the FD, i.e., from November 4 at 12:00 UTC to November 5 at 00:00 UTC, and the associated spectrum obtained from the model with the 12 hr averaged  $\phi = [432 \pm 3]$  MV. As clearly shown in Figure 8, they are in very good agreement. In this figure, we report the background spectrum in blue and the proton spectrum at the dip of the FD in orange. Circles indicate HEPD-01 observations with error bars and superposed solid lines indicate model prediction.

Taking into account the variations in the count rates observed by the HET and HEPD-01 count rates, we can compare the observed FD amplitude with the amplitude estimated using the model with the modulation potential  $\phi$  fitted to the NM data. We calculate the variations

$$\frac{\Delta N}{N_0} = \left[ 1 - \frac{\sum_s \int_{E_0}^{E_1} J_s(E, \phi) dE}{\sum_s \int_{E_0}^{E_1} J_{0,s}(E, \phi_0) dE} \right] \times 100, \quad (6)$$

where  $E_0 = 10$  MeV and  $E_1 = 300$  MeV are representative of the energy range of the HEPD-01 detector and also match the HET sensitivity range (J. Rodríguez-Pacheco et al. 2020). Since the aim is to compare model results with space-based observations, the anisotropy factor  $\mathcal{A}$  and the NM response function  $W_c$  are not included in Equation (6). The results are shown in Figure 9, where the predicted modulation is consistent with both data samples within error bars. In fact, the tendency toward a flat trend predicted by the analytic expression (6) has been observed in the amplitudes observed by the two spacecraft.

## 5.2. GCR Anisotropy

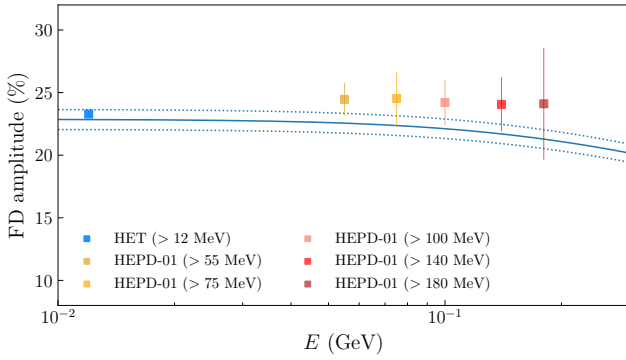
The bottom panels of Figure 7 display the magnitude of first- and second-order anisotropies as a function of time, whose amplitudes have been calculated as

$$A_1 = \sqrt{\sum_{m=-1}^1 a_{1m}^2}, \quad A_2 = \sqrt{\sum_{m=-2}^2 a_{2m}^2}. \quad (7)$$

We observe a pronounced increase of both anisotropic contributions during the MFR passage, where the second-

<sup>10</sup> <https://omniweb.gsfc.nasa.gov/form/dx1.html>





**Figure 9.** Comparison between the FD amplitude predicted by the model (solid line) with  $\phi = [432 \pm 3]$  MV and space-based observations (squares). Dotted lines indicate the model uncertainty. Space-based observations are HET (blue) and HEPD-01 ratemeters in five channels (from yellow to red).

order term tends to dominate the other, implying the presence of a bidirectional anisotropy associated with the magnetic structure. This is evident in Figure 10, where we depict the two contributions during the closest approach to the MFR core of SO and Wind at 19:30 in the GSE reference frame. The locations of the two anisotropy sources are compared with the directions parallel/antiparallel to the IMF and the MFR axis through the GS reconstruction. The MFR axis direction is inclined of  $38.5^\circ$  with respect to the total IMF. Although a particle flux parallel or antiparallel to the MFR axis might play an important role in determining the GCR anisotropy, in this case the best match is obtained with the IMF directions. This will be discussed in the next section in terms of the median energy of GCR particles detected by NMs.

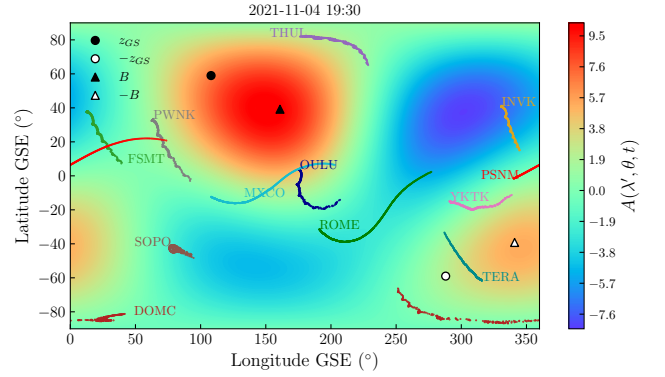
### 5.3. Model Performance

Before proceeding with the discussion, we illustrate the model performance for the case study of the 2021 November 4 FD. Due to the large anisotropy of the event, the maximum amplitude of the FD is reached at different times from different groups of NM stations, depending on their geographic position and therefore on their directions of viewing. We then selected the maximum amplitude time bin at each station, and then we reconstructed the predicted FD amplitude by using the optimal model parameters obtained from the fit. A comparison between the observed and predicted FD amplitude is shown in Figure 11 as a function of the cutoff rigidity (color map). The agreement between the amplitudes predicted by the model and ground-based observations is remarkable, since the data points align along the bisector line. To quantify the quality of the FD profiles reconstructed by the model, we calculated the  $R^2$ -score

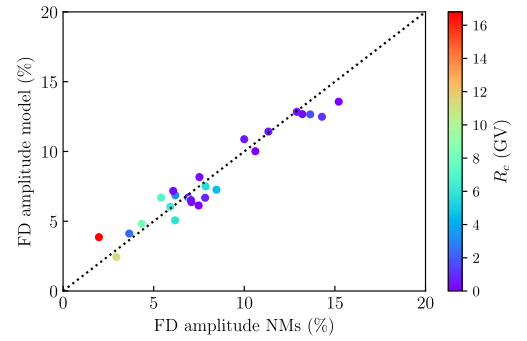
$$R^2 = 1 - \frac{\sum_{k=1}^{n_p} (I_{t_k} - \hat{I}_{t_k})^2}{\sum_{k=1}^{n_p} (I_{t_k} - \langle I \rangle)^2}, \quad (8)$$

where  $I$ ,  $\hat{I}$ , and  $\langle I \rangle$  are the observed, modeled, and averaged GCR intensity variations, respectively, and  $n_p$  is the number of data points in the time series. We then calculated the root mean squared error (RMSE) defined as

$$\text{RMSE} = \sqrt{\frac{\sum_{k=1}^{n_p} (I_{t_k} - \hat{I}_{t_k})^2}{n_p}}. \quad (9)$$



**Figure 10.** Anisotropy map obtained at the closest approach to the MFR core on November 4 at 19:30 UT. The colored dots indicate the asymptotic directions of a subset of the NMs used in the study. The filled (empty) circle indicates the parallel (antiparallel) direction to the MFR axis. The filled (empty) triangle denotes the parallel (antiparallel) direction to the IMF.



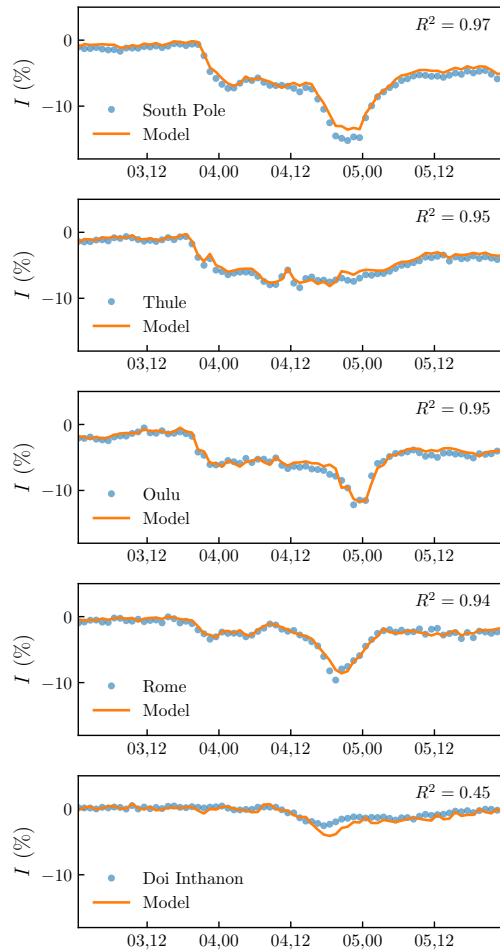
**Figure 11.** Scatter plot between the observed and predicted maximum FD amplitude. The color map indicates the cutoff rigidity  $R_c$  of each NM station.

These performance metrics quantify the goodness of the retrieval of the target time series (observed GCR intensity variations) achieved by the model. The results showing the comparison between observed cosmic-ray variations and model predictions for a few NMs with different cutoff rigidities are shown in Figure 12. The  $R^2$ -score and the RMSE obtained for all the NMs used in the study are listed in Table 2. The high values of the  $R^2$ -score and the  $\text{RMSE} < 1\%$  show that the model accurately reproduces the observed GCR intensity variations.

## 6. Summary and Discussion

In this work, we analyzed the first large FD of Solar Cycle 25 from a multipoint perspective. We compared magnetic field and plasma measurements gathered by SO at 0.82 au and Wind at L1, where the large-scale MFR structure has been clearly identified. We used the GS reconstruction to infer the spatial geometry of the MFR by using Wind data and SO magnetic field observations to perform a validation of the outcomes. Then, we compared GCR intensities obtained from the integrated counts of HET on SO, the ratemeters of HEPD-01 on board CSES-01, and ground-based NM observation. The large amplitude of the FD observed at the ground, its strong anisotropy, along with the availability of differential proton spectra on HEPD-01 in the sub-GeV range, allowed us to model the FD and to retrieve the main characteristics by using the NM network: (i) the primary proton spectrum and (ii) the cosmic-ray anisotropy. Taking advantage of the HEPD-01





**Figure 12.** Comparison between GCR percentage variations as observed by a subset of NMs placed at different geographic positions (circles) and the relative model outcomes (solid lines).

energy range, we modeled the GCR spectrum using the mathematical expression provided by the G&A model. In this framework, the force-field approximation was not invoked, being invalid over short timescales in disturbed heliospheric conditions. The effectiveness of such a model in capturing the main characteristics of also short-term modulations of the differential GCR spectrum during FD events has been pointed out by I. G. Usoskin et al. (2015) by comparing the modulation potential retrieved through the NM network with that obtained by fitting with the G and A model the primary spectra of protons and Helium nuclei observed by the Payload for Antimatter Matter Exploration and Light-nuclei Astrophysics (PAMELA) as a function of time. In this work, we extended these results to the lower energy range covered by HEPD-01, showing that the force-field parameterization is also effective in reproducing observations at these energies.

The first step of the FD, associated with the passage of the interplanetary shock and the turbulent sheath region, is found to be characterized by an almost isotropic depression of the GCR intensity, since the GCR anisotropy does not exhibit a significant increase in crossing the shock-sheath region. The same conclusions have been pointed out by K. Munakata et al. (2022) on the basis of a larger sample of data including NMs and muon detectors, and by P. Gololobov et al. (2023), who applied the global-survey method to derive omnidirectional particle density and first-order anisotropy. However,

**Table 2**  
 $R^2$ -score and RMSE Obtained for Each NM Stations

NM Station	$R^2$ -score	RMSE (%)
Terre Adelie	0.93	0.60
Dome C	0.95	0.71
South Pole	0.97	0.71
Nain	0.92	0.66
Jang Bogo	0.94	0.57
Inuvik	0.97	0.61
Thule	0.95	0.52
Fort Smith	0.98	0.48
Peawanuck	0.95	0.54
Tixie Bay	0.98	0.55
Norilsk	0.92	0.89
Apatity	0.95	0.54
Oulu	0.95	0.54
Kerguelen	0.95	0.70
Yakutsk	0.96	0.62
Newark	0.90	0.69
Dourbes	0.93	0.62
Jungfrau-joch	0.88	0.88
Baksan	0.93	0.60
Almaty	0.87	0.74
Rome	0.94	0.46
Calma	0.87	0.60
Mexico	0.85	0.63
Athens	0.90	0.51
Daejeon	0.60	0.73
Doi Inthanon	0.45	0.59

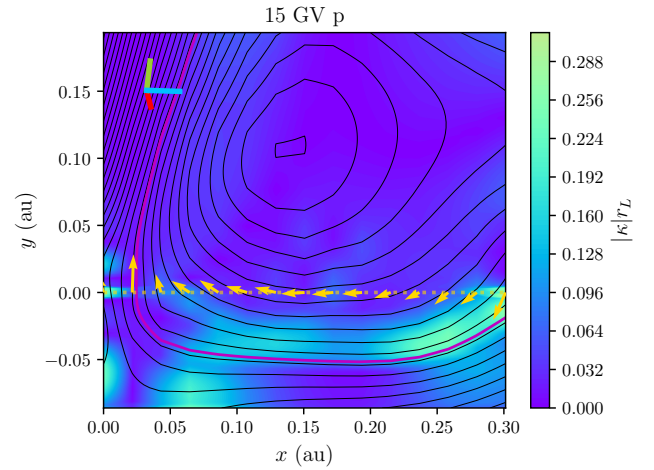
observations of the time evolution of GCR spectrum based on the ORCA (Antarctic Cosmic Ray Observatory) display some degree of anisotropy associated with the west-east difference of the incoming muons in the shock/sheath time interval (J. J. Blanco et al. 2024). A transient anisotropy during this time period, near the end of the turbulent sheath region, has also been reported in TeV-range observations from the Large High Altitude Air Shower Observatory (K. Koenonk et al. 2024).

The second step of the FD, corresponding to the MFR passage, is found to be highly anisotropic, with strong evidence of bidirectional GCR anisotropy aligned with the IMF parallel and antiparallel directions during the FD main phase, as also reported in K. Munakata et al. (2022). The anisotropy map in our Figure 10 derived from NM data is visually very similar to that shown for the same time (19:30 UT) in Figure 4 of K. Munakata et al. (2022), which was derived from both NM and muon detector data, showing that our use of NM data alone results in a very similar pattern. By inspecting the time of the FD main phase and the corresponding configuration of the MFR, we observed that the maximum amplitude of the FD occurs in correspondence of the SO and Wind closest approach to the MFR core region. The GS reconstruction allowed us to estimate the “impact factor” of the MFR, which in this case is approximately 0.11 au. Despite its large value, the axial component is the strongest, being the IMF vector closely aligned along the axial direction. Hence, the dominant axial component and the weak particle scattering can support the occurrence of a bidirectional GCR anisotropy. Otherwise, a significant population of GCR particles around the IMF direction cannot be easily maintained (K. Munakata et al. 2022). Moreover, the “impact factor” provided by the GS reconstruction is typically subject to large uncertainties and the goodness of multispacecraft validations, such as the one

performed by using Wind and SO, is the only way of having information about the actual MFR “impact factor.”

Concerning particle trapping, the sudden drop in the IMF fluctuations  $\delta B$  and the resulting smooth rotation of the MFR over an extended time interval suggest a reduction of the pitch-angle scattering effect (W. Krittinatham & D. Ruffolo 2009; O. Pezzi et al. 2022, 2024). In this case, GCR particles with pitch angles close to parallel and antiparallel directions to the IMF can be maintained for a reasonable amount of time. Sources for particle injection for the subsequent MFR confinement are the cross-field diffusion of particles following the MFR field or the direct propagation of particles toward the isolated field lines through finite Larmor radius effect, as shown, e.g., by T. Laitinen & S. Dalla (2021) through test-particle simulations with both full-orbit and particle diffusion approaches. Moreover, according to Y. Kubo & H. Shimazu (2010) GCR particle diffusion is the dominant process when MFRs are close to the Sun, whereas the gyration is the dominant one at Earth. These models are based on cylindrical MFRs, thus having a geometry assumption which resembles the one of the GS reconstruction employed in the present study. However, the whole MFR configuration encompassing the geometry of its legs plays a significant role in particle entering and trapping. W. Krittinatham & D. Ruffolo (2009) demonstrated that cosmic-ray particles can penetrate the MFR from the legs through drift. However, this mechanism alone is expected to produce a net unidirectional GCR flux in a direction parallel or antiparallel to the MFR axis, depending on the sense of rotation of the poloidal magnetic field. The occurrence of such unidirectional anisotropy has been supported by observations in the event studied by U. Tortermun et al. (2018), but also countered in the event studied by W. Kihara et al. (2021), where the unidirectional anisotropy develops in the opposite direction with respect to the prediction made by W. Krittinatham & D. Ruffolo (2009). In the event analyzed in this work, the bidirectional anisotropy observed challenges this theoretical prediction, since given the geometry of the poloidal field (e.g., see the right panel of Figure 4) we would expect a net unidirectional flux of GCR particles flowing along a direction antiparallel to the MFR axis. In this regard, the injection and trapping mechanisms associated with the global configuration of the ICME contribute to the formation of the GCR particle population observed in directions close to  $0^\circ$ – $180^\circ$  to the IMF or possibly to the MFR axis, depending on the magnetic field configuration and particle energies.

We observed that the GCR anisotropy is well aligned with IMF parallel-antiparallel directions, and less with the MFR axis. This may be related to the energy of the particle population detected by NMs. If we consider protons with a median energy of 15 GV as representative of the NM counts (see, for instance, K. Munakata et al. 2022), we can estimate the associated Larmor radius  $r_L$  inside the MFR by using the quasi-three-dimensional GS reconstruction. We then calculate the curvature of the magnetic field  $|\kappa| = |\mathbf{b} \cdot \nabla \mathbf{b}| = R_{\text{curv}}^{-1}$ , where  $\mathbf{b}$  denotes the magnetic field unit vector, and  $R_{\text{curv}}$  is the curvature radius of the magnetic field. We compared the size of the Larmor radius with  $R_{\text{curv}}$  through the parameter  $|\kappa|r_L$  at all points on the map. As shown in Figure 13, the product  $|\kappa|r_L \ll 1$  is close to the core of the MFR at the Earth’s location for 15 GV protons, suggesting that at these rigidities the particles are strongly affected by the magnetic field



**Figure 13.** Map of the  $|\kappa|r_L$  parameter inside the MFR. The black curves indicate the magnetic field vector potential. The horizontal dashed line is the Wind spacecraft path through the MFR along with magnetic field measurements (yellow arrows). In the corner, we show a projection of the GSE reference frame.









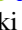



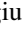

curvature. In this scenario, cosmic-ray particles tend to move preferentially along the field lines, producing the IMF-aligned anisotropy observed in the NM data.

In summary, we showed that the force-field parameterization of the primary GCR flux allows us to describe the evolution of FDs in the sub-GeV energy range. We retrieved the MFR configuration from plasma measurements and found a clear correspondence between the configuration of the MFR, the IMF direction, and the GCR anisotropy. Further investigation based on both FD observations and numerical simulations are needed to assess the role of the different mechanisms in filling the large-scale MFRs of solar origin and producing bidirectional anisotropies such as the one observed in the 2021 November 4 event.

### Acknowledgments

This work uses data from the CSES mission, funded by the China National Space Administration (CNSA) and the China Earthquake Administration (CEA) in collaboration with the Italian Space Agency (ASI), the National Institute for Nuclear Physics (INFN), the Institute for Applied Physics (IFAC-CNR), and the Institute for Space Astrophysics and Planetology (INAF-IAPS). This work is partly supported by the Italian Space Agency in the framework of the “Accordo Attuativo 2020-32.HH.0 Limadou Scienza+” (CUP F19C20000110005), the ASI-INFN Agreement No. n.2014-037-R.0, addendum 2014-037-R-1-2017, and the ASI-INFN Agreement No. 2021-43-HH.0. This research received funding from the European Union’s Horizon Europe program under grant agreement No. 101135044 (SPEARHEAD, <https://spearhead-he.eu/>). Support in Thailand has been provided by the National Science and Technology Development Agency (NSTDA) and the National Research Council of Thailand (NRCT) under the High-Potential Research Team Grant Program (N42A650868). We acknowledge the use of the OTSO tool (Version 1.4), the GitHub repository of which can be found at <https://github.com/NLarsen15/OTSO> (N. Larsen & C. T. Steigies 2024). We acknowledge the NMDB database ([www.nmdb.eu](http://www.nmdb.eu)) funded under the European Union’s FP7 program (contract No. 213007), and the PIs of individual NM stations for providing data.

## ORCID iDs

Simone Benella  <https://orcid.org/0000-0002-7102-5032>  
 Monica Laurenza  <https://orcid.org/0000-0001-5481-4534>  
 Matteo Martucci  <https://orcid.org/0000-0002-3033-4824>  
 David Ruffolo  <https://orcid.org/0000-0003-3414-9666>  
 Qiang Hu  <https://orcid.org/0000-0002-7570-2301>  
 Georgios Nicolaou  <https://orcid.org/0000-0003-3623-4928>  
 Christopher J. Owen  <https://orcid.org/0000-0002-5982-4667>  
 Mirko Stumpo  <https://orcid.org/0000-0002-6303-5329>  
 Christina Plainaki  <https://orcid.org/0000-0003-1483-5052>  
 Francesco Palma  <https://orcid.org/0000-0001-7076-8830>  
 Mirko Piersanti  <https://orcid.org/0000-0001-5207-2944>  
 Matteo Sorbara  <https://orcid.org/0000-0002-3996-0370>  
 Alessandro Sotgiu  <https://orcid.org/0000-0001-8835-2796>  
 Roberta Sparvoli  <https://orcid.org/0000-0002-6314-6117>

## References

- Alken, P., Thébault, E., Beggan, C. D., et al. 2021, *EP&S*, **73**, 49  
 Aran, A., Pacheco, D., Laurenza, M., et al. 2021, *A&A*, **656**, L10  
 Bartocci, S., Battiston, R., Burger, W. J., et al. 2020, *ApJ*, **901**, 8  
 Belov, A. V., Eroshenko, E. A., Yanke, V. G., et al. 2018, *Ge&Ae*, **58**, 356  
 Benella, S., Laurenza, M., Vainio, R., et al. 2020, *ApJ*, **901**, 21  
 Benella, S., Laurenza, M., Vainio, R., et al. 2021, in Proc. 1st Virtual Symp. on Cosmic Ray Studies with Neutron Detectors (NMDB@Home 2020), ed. M. Abunina, R. Bütkofer, K. L. Klein et al. (Kiel: Kiel Univ. Publishing), 49  
 Bieber, J. W., Dröge, W., Evenson, P. A., et al. 2002, *ApJ*, **567**, 622  
 Bieber, J. W., & Evenson, P. 1998, *GeoRL*, **25**, 2955  
 Blanco, J. J., Ayuso, S., Regadio, A., et al. 2024, *AdSpR*, **73**, 4842  
 Bombardieri, D. J., Duldig, M. L., Michael, K. J., & Humble, J. E. 2006, *ApJ*, **644**, 565  
 Burlaga, L. F., Klein, L., Sheeley, N. R., J., et al. 1982, *GeoRL*, **9**, 1317  
 Burlaga, L. F. E. 1991, in Physics of the Inner Heliosphere II, ed. R. Schwenn & E. Marsch, Vol. 21 (Berlin: Springer), 1  
 Caballero-Lopez, R. A., & Moraal, H. 2004, *JGRA*, **109**, A01101  
 Cane, H. V. 2000, *SSRv*, **93**, 55  
 Cane, H. V., Richardson, I. G., von Rosenvinge, T. T., & Wibberenz, G. 1994, *JGR*, **99**, 21429  
 Chiappetta, F., Laurenza, M., Lepreti, F., et al. 2023, *FrASS*, **10**, 1209479  
 Cramp, J. L., Duldig, M. L., Flückiger, E. O., et al. 1997, *JGR*, **102**, 24237  
 de Hoffmann, F., & Teller, E. 1950, *PhRv*, **80**, 692  
 Dumbović, M., Heber, B., Vršnak, B., Temmer, M., & Kirin, A. 2018, *ApJ*, **860**, 71  
 Forbush, S. E. 1937, *PhRv*, **51**, 1108  
 Freiherr von Forstner, J. L., Dumbović, M., Möstl, C., et al. 2021, *A&A*, **656**, A1  
 Freiherr von Forstner, J. L., Guo, J., Wimmer-Schweingruber, R. F., et al. 2018, *JGRA*, **123**, 39  
 Gieseler, J., Dresing, N., Palmroos, C., et al. 2023, *FrASS*, **9**, 384  
 Gleeson, L. J., & Axford, W. I. 1968, *ApJ*, **154**, 1011  
 Gololobov, P., Grigoryev, V., Gerasimova, S., et al. 2023, in Proc. Hybrid Symp. on Cosmic Ray Studies with Neutron Detectors (NMDB@Athens), ed. R. Bütkofer, A. Gil-Šwidarska, K. L. Klein et al. (Kiel: Kiel Univ. Publishing), 27  
 Hau, L. N., & Sonnerup, B. U. Ö. 1999, *JGR*, **104**, 6899  
 Horbury, T. S., O'Brien, H., Carrasco Blazquez, I., et al. 2020, *A&A*, **642**, A9  
 Hu, Q., & Sonnerup, B. U. Ö. 2002, *JGRA*, **107**, 1142  
 Hu, S. Q. 2017, *ScChD*, **60**, 1466  
 Iucci, N., Parisi, M., Signorini, C., Storini, M., & Villaresi, G. 1989, *A&AS*, **81**, 367  
 Jordan, A. P., Spence, H. E., Blake, J. B., & Shaul, D. N. A. 2011, *JGRA*, **116**, A11103  
 Kihara, W., Munakata, K., Kato, C., et al. 2021, *SpWea*, **19**, e02531  
 Koennonkok, K., Ruffolo, D., Mithumsiri, W., Liu, W., & Lhaaso Collaboration 2024, ICRC (Nagoya), **38**, 1300  
 Krittianatham, W., & Ruffolo, D. 2009, *ApJ*, **704**, 831  
 Kubo, Y., & Shimazu, H. 2010, *ApJ*, **720**, 853  
 Kuwabara, T., Bieber, J. W., Evenson, P., et al. 2009, *JGRA*, **114**, A05109  
 Laitinen, T., & Dalla, S. 2021, *ApJ*, **906**, 9  
 Larsen, N., Mishev, A., & Usoskin, I. 2023, *JGRA*, **128**, e2022JA031061  
 Larsen, N., & Steigies, C. T. 2024, NLarsen15/OTSO: OMNI Data, v1.4.0, Zenodo, doi:10.5281/zenodo.14179975  
 Lepping, R. P., Acuña, M. H., Burlaga, L. F., et al. 1995, *SSRv*, **71**, 207  
 Lockwood, J. A., Webber, W. R., & Debrunner, H. 1991, *JGR*, **96**, 5447  
 Martucci, M., Ammendola, R., Badoni, D., et al. 2023b, *ApJL*, **945**, L39  
 Martucci, M., Bartocci, S., Battiston, R., et al. 2022, *PhRvD*, **105**, 062001  
 Martucci, M., Laurenza, M., Benella, S., et al. 2023a, *SpWea*, **21**, e2022SW003191  
 Mishev, A., Larsen, N., Asvestari, E., et al. 2024, *AdSpR*, **74**, 4160  
 Mishev, A., Usoskin, I., Raukunen, O., et al. 2018, *SoPh*, **293**, 136  
 Mishev, A. L., Kocharov, L. G., Koldobskiy, S. A., et al. 2022, *SoPh*, **297**, 88  
 Mishev, A. L., Kocharov, L. G., & Usoskin, I. G. 2014, *JGRA*, **119**, 670  
 Mishev, A. L., Koldobskiy, S. A., Kovaltsov, G. A., Gil, A., & Usoskin, I. G. 2020, *JGRA*, **125**, e27433  
 Möstl, C., Farrugia, C. J., Biernat, H. K., et al. 2009, *SoPh*, **256**, 427  
 Munakata, K., Bieber, J. W., Yasue, S.-i., et al. 2000, *JGR*, **105**, 27457  
 Munakata, K., Yasue, S., Kato, C., et al. 2006, in Advances in Geosciences, Volume 2: Solar Terrestrial (ST), ed. M. Duldig (Singapore: World Scientific), 115  
 Munakata, K., Kozai, M., Kato, C., et al. 2022, *ApJ*, **938**, 30  
 Ogilvie, K. W., Chornay, D. J., Fritzenreiter, R. J., et al. 1995, *SSRv*, **71**, 55  
 Owen, C. J., Bruno, R., Livi, S., et al. 2020, *A&A*, **642**, A16  
 Papailiou, M., Abunina, M., Belov, A., et al. 2020, *SoPh*, **295**, 164  
 Papaioannou, A., Kouloumvakos, A., Mishev, A., et al. 2022, *A&A*, **660**, L5  
 Paularena, K. I., Wang, C., von Steiger, R., & Heber, B. 2001, *GeoRL*, **28**, 2755  
 Petukhova, A. S., Petukhov, I. S., & Petukhov, S. I. 2019, *ApJ*, **880**, 17  
 Pezzi, O., Blasi, P., & Matthaeus, W. H. 2022, *ApJ*, **928**, 25  
 Pezzi, O., Trotta, D., Benella, S., et al. 2024, *A&A*, **686**, A116  
 Picozza, P., Battiston, R., Ambrosi, G., et al. 2019, *ApJS*, **243**, 16  
 Plainaki, C., Mavromichalaki, H., Belov, A., Eroshenko, E., & Yanke, V. 2009, *AdSpR*, **43**, 474  
 Plainaki, C., Mavromichalaki, H., Laurenza, M., et al. 2014, *ApJ*, **785**, 160  
 Potgieter, M. S. 2013, *LRSP*, **10**, 3  
 Rodríguez-Pacheco, J., Wimmer-Schweingruber, R. F., Mason, G. M., et al. 2020, *A&A*, **642**, A7  
 Shea, M. A., & Smart, D. F. 1982, *SSRv*, **32**, 251  
 Shen, X., Zhang, X. M., Yuan, S. G., et al. 2018, *ScChE*, **61**, 634  
 Simpson, J. A. 2000, *SSRv*, **93**, 11  
 Tortermpun, U., Ruffolo, D., & Bieber, J. W. 2018, *ApJL*, **852**, L26  
 Tsyganenko, N. A. 2002a, *JGRA*, **107**, 1179  
 Tsyganenko, N. A. 2002b, *JGRA*, **107**, 1176  
 Tsyganenko, N. A., Singer, H. J., & Kasper, J. C. 2003, *JGRA*, **108**, 1209  
 Usoskin, I. G., Gil, A., Kovaltsov, G. A., Mishev, A. L., & Mikhailov, V. V. 2017, *JGRA*, **122**, 3875  
 Usoskin, I. G., Kovaltsov, G. A., Adriani, O., et al. 2015, *AdSpR*, **55**, 2940  
 Wibberenz, G., & Cane, H. V. 2000, *JGR*, **105**, 18,315  
 Wibberenz, G., Le Roux, J. A., Potgieter, M. S., & Bieber, J. W. 1998, *SSRv*, **83**, 309  
 Winslow, R. M., Schwadron, N. A., Lugaz, N., et al. 2018, *ApJ*, **856**, 139  
 Witasse, O., Sánchez-Cano, B., Mays, M. L., et al. 2017, *JGRA*, **122**, 7865